

CrossMark
click for updatesCite this: *RSC Adv.*, 2014, 4, 31782

Functionalized graphene oxide/phosphoramidate oligomer hybrids flame retardant prepared *via in situ* polymerization for improving the fire safety of polypropylene†

Bin Yu,^{ab} Xin Wang,^a Xiaodong Qian,^{ab} Weiyi Xing,^a Hongyu Yang,^{ab} Liyan Ma,^a Ying Lin,^a Saihua Jiang,^{ab} Lei Song,^a Yuan Hu^{*ab} and Siuming Lo^{bc}

A novel strategy based on functionalized graphene oxide (FGO)/phosphoramidate oligomer flame retardant was developed to overcome the challenges of the dispersion of graphene sheets in polymer matrix and the ease of the burn-out of graphene under air atmosphere. Graphene oxide (GO) was modified by 4,4-diaminodiphenyl methane (DDM) and then *in situ* incorporated into phosphoramidate oligomer, resulting in a nanocomposite flame retardant (FRs-FGO) containing exfoliated graphene. Subsequently, the flame retardant (FRs-FGO) was incorporated into polypropylene (PP) and simultaneously compatibilized with PP-grafted maleic anhydride. TEM results showed that the FGO was dispersed more uniformly in PP than the bare GO because of the strong interfacial interaction and previous exfoliation of FGO in FRs before blending. The thermal properties investigated by thermogravimetric analysis (TGA) indicated that the addition of FRs-FGO into PP resulted in a significant improvement of thermal stability at elevated temperature with higher char yields. Moreover, the crystallization and fire safety properties of PP composites were also improved by the incorporation of FRs-FGO, including increased crystallization temperature (11.4 °C increase), reduced peak heat release rate (66.9% reduction) and decreased total heat release (24.4% decrease), and decreased fire growth rate index (73.0% decrease). The cone results indicated the simple blending of GO with FRs and exhibited less improvement in fire safety properties than FRs-FGO, which resulted from the improved dispersion and thermal stability of FGO sheets. The flame retardant mechanism was because of the shielding effect of FGO and char layers, which could reduce the release of combustible gases and inhibit the mass and heat transfer between the gas phase and condensed phase.

Received 19th October 2013
Accepted 9th June 2014

DOI: 10.1039/c3ra45945d

www.rsc.org/advances

1. Introduction

In today's society, organic polymers are extensively used in different fields, including electronics, coatings, cable, *etc.*, because of their excellent properties such as low density, resistance to erosion, ease of processing, *etc.*^{1,2} However, the intrinsic flammability of polymers, which has resulted in huge loss of human lives and property, limits their use in some areas. Thus, it is necessary and urgent to make commercial polymers

non-flammable or flame-retardant. Among various halogen-free FRs, intumescent flame retardants (IFRs) have been proven to be effective flame retardants for thermoplastic resins such as PP and poly-ethylene (PE), and are widely used in the industrial applications.³⁻⁵ In general, a typical intumescent flame retardant (IFR) system consists of three main components, namely an acid source, a char-forming agent and a blowing agent.⁶ However, the IFR systems containing an APP and two other basic components are hardly evenly dispersed in the matrix according to the addition ratio, thus the flame retardant efficiency of these systems is reduced. Thus, some researchers have been exploring novel IFRs with these three basic components on a small molecular compound or oligomer.⁷⁻⁹ However, a fairly high loading is usually required to achieve good fire resistance that will deteriorate the physical and mechanical properties of the polymeric materials. Therefore, to improve the flame retardant efficiency and reduce the amounts of IFRs used in polymers, the combination of nano technology and the IFR strategy has been adopted.

^aState Key Laboratory of Fire Science, University of Science and Technology of China, 96 Jinzhai Road, Hefei, Anhui 230026, P.R. China. E-mail: yuanhu@ustc.edu.cn; Fax: +86-551-3601664; Tel: +86-551-3601664

^bUSTC-CityU Joint Advanced Research Centre, Suzhou Key Laboratory of Urban Public Safety, Suzhou Institute for Advanced Study, University of Science and Technology of China, 166 Ren'ai Road, Suzhou, Jiangsu 215123, P.R. China

^cDepartment of Building and Construction, City University of Hong Kong, Tat Chee Avenue Kowloon, Hong Kong

† Electronic supplementary information (ESI) available. See DOI: 10.1039/c3ra45945d

Graphene, a one-atom-thick, two-dimensional (2-D) sheet composed of sp^2 carbon atoms in a hexagonal lattice, has attracted wide attention from both scientific and industrial fields because of its exceptional electronic, thermal and mechanical properties.^{10–13} With these fascinating properties, graphene has motivated tremendous interest in preparing graphene-based polymer composites. Recently, graphene with a unique sheet structure, similar to the layered silicate, has been used as a flame-retardant additive in polymer nanocomposites.^{14–16} The huge challenge for the applications of graphene/polymer nanocomposites at present is the dispersion of graphene in the polymer matrix due to the intrinsic van der Waals force between graphene sheets, which results in the re-aggregating and restacking of graphene.^{17–19} Moreover, the bare graphene is easily burnt out upon exposure to a heat flow under air atmosphere, which could not act as an effective barrier to prevent the escape of organic volatiles. The chemical modification of graphene with flame retardants is a better choice because of the existing functional groups (hydroxyl and carboxyl) on the basal plane and edges of graphene, which can provide reactive sites for chemical functionalization.^{20–22} The flame-retardant elements on the surface of graphene can not only facilitate the dispersion of graphene but also generate some char layers during combustion, as suggested by our previous work.²³ Unfortunately, the previous studies have demonstrated that the amount of oxygen-containing groups on the surface of graphene was limited (oxygen atom percentage of approximately 30% for graphene oxide), and thus only limited flame retardants could be grafted onto graphene.^{24,25} To address this problem, a novel strategy of graphene wrapped with large amounts of flame retardants is emerging, which can broaden the applications of polymer/graphene nanocomposites for fire retardancy.

Presently, the dispersion of graphene in polymers is carried out by three methods, namely *in situ* polymerization, solvent blending and melt blending. Melt blending lead to poor dispersion, whereas *in situ* polymerization and solvent blending usually result in good dispersion. The combination of nanocomposite technology and the IFR strategy is generally achieved by the melt blending method, but rarely *via in situ* polymerization method. As a result, new ideas regarding phosphoramidate oligomer nanocomposite FR containing exfoliated and reduced graphene oxide sheets *via in situ* polymerization, aiming at improving the dispersion and interfacial interactions in polymer matrix, is suggested.

Polypropylene (PP), one of the most widely used thermoplastic materials, has been used in several fields, such as furniture, electric casings, electronics, interior decorations, insulation, because of its low density, easy process property, chemical resistance, *etc.*^{26–28} However, PP is highly flammable and drips during combustion. Moreover, it emits smoke and poisonous gases while burning, which limits the range of its applications, especially in fields where high flame retardancy is required such as electrical industries.^{4,29} Therefore, the reduction of the fire hazards of PP and expansion of its application in some limited fields are rather imperative and significant.

In the present work, a kind of phosphoramidate oligomer nanocomposite FR containing exfoliated and reduced graphene oxide (FRs-FGO) was successfully prepared *via in situ* polymerization. Then, FRs-FGO was incorporated into PP to obtain the flame retardant PP nanocomposites. To further improve the dispersion and compatibility of both graphene oxide and FR in the PP matrix, PP-grafted maleic anhydride (PP-*g*-MA) was used as a compatilizer. Graphene oxide was firstly treated in the presence of 4,4-diaminodiphenyl methane. The structure and morphology of FGO was characterized by FTIR, XPS, XRD and TEM. The crystallization, thermal and combustion properties of PP nanocomposites were investigated by DSC, TGA, cone tests, and the flame retardant mechanism was discussed.

2. Experimental

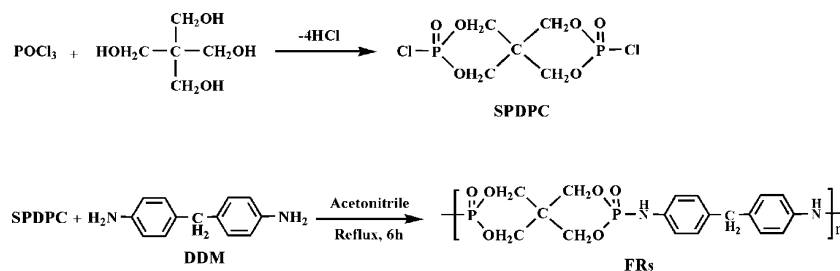
2.1 Raw materials

PP (homopolymer, melt-flow rate = 2.5 g/10 min) was supplied by Yangzi Petrochemical Co., Ltd. (China). PP-grafted maleic anhydride (PP-*g*-MA, 0.6–1.0 MA%) was purchased from Ningbo Nengzhiguang New Materials Technology Co., Ltd. 4,4-Diamino-diphenyl methane (DDM) was purchased from Sino-pharm Chemical Reagent Co. Ltd. (Shanghai, China). Reagent grade phosphorus oxychloride was provided by Shanghai HuaYi Group HuaYuan Chemical Industry Co. Ltd. (Shanghai, China). Pentaerythritol, acetonitrile, trichloromethane and diethyl ether, *N,N*-dimethylformamide (DMF, AP), graphite powder, potassium permanganate ($KMnO_4$, AP), hydrochloric acid (HCl, CP), sulfuric acid (H_2SO_4 , 98%), sodium nitrate ($NaNO_3$, AP), hydrogen peroxide (H_2O_2 , 30% aq.) and hydrazine hydrate (85%, AP) were all reagent grade and purchased from Sinopharm Chemical Reagent Co. Ltd. (Shanghai, China).

2.2 Preparation of FRs and FRs-FGO nanocomposite flame retardants

Spirocyclic pentaerythritol bisphosphorate disphosphoryl chloride (SPDPC) was prepared in our group³⁰ and poly-(diaminodiphenyl methane spirocyclic pentaerythritol bisphosphonate) (FRs) was prepared according to the reported method, as shown in Scheme 1.³¹ Typically, SPDPC (30 g, 0.101 mol) and DDM (20.8 g, 0.105 mol) were added in a glass flask and dispersed by acetonitrile (150 ml). The mixture was stirred and gradually heated under nitrogen protection. The reaction was completed after 6 h at 80 °C, when no HCl could be detected. The obtained product was filtered and purified with acetonitrile and then dried to a constant weight at 80 °C in a vacuum oven. The pale yellow solid powder was obtained (yield: 92%).

Graphite oxide was prepared from graphite powder using a modified Hummers' method.³² GO was modified and reduced by DDM and the preparation process was as follows. Briefly, 1.0 g of graphite oxide was dispersed in 300 ml DMF by ultrasonication for 60 min at room temperature. Then, the obtained suspension was introduced into a 500 ml three-necked flask equipped with a nitrogen inlet, mechanical stirrer and reflux condenser. Subsequently, 3.0 g of DDM were added to the flask and the reaction was conducted under nitrogen at 90 °C for



Scheme 1 Synthetic route of poly(4,4-diaminodiphenyl methane spirocyclicpentaerythritol bisphosphonate) (FRs).

24 h. After the completion of this reaction, the slurry mixture was filtered through a 0.2 μm polytetrafluoroethylene membrane and thoroughly washed with DMF and trichloromethane to remove the residual reagent. The filtercake was dried under vacuum at 80 °C overnight. The preparation procedure of FRs-FGO nanocomposite flame retardants is illustrated in Scheme 2. FGO (1.0 g) was dispersed in anhydrous acetonitrile (100 ml) with sonication for 1 h, leading to the formation of a homogeneous suspension. Then, SPDPC (7.05 g) and DDM (4.88 g) were charged into the abovementioned suspension and the reaction mixture was refluxed and stirred at 80 °C under a nitrogen atmosphere until no HCl was emitted. The FRs-FGO nanocomposite was filtered and washed with acetonitrile for three times. Finally, the filter cake was collected by overnight drying at 80 °C in a vacuum oven (yield: 87%).

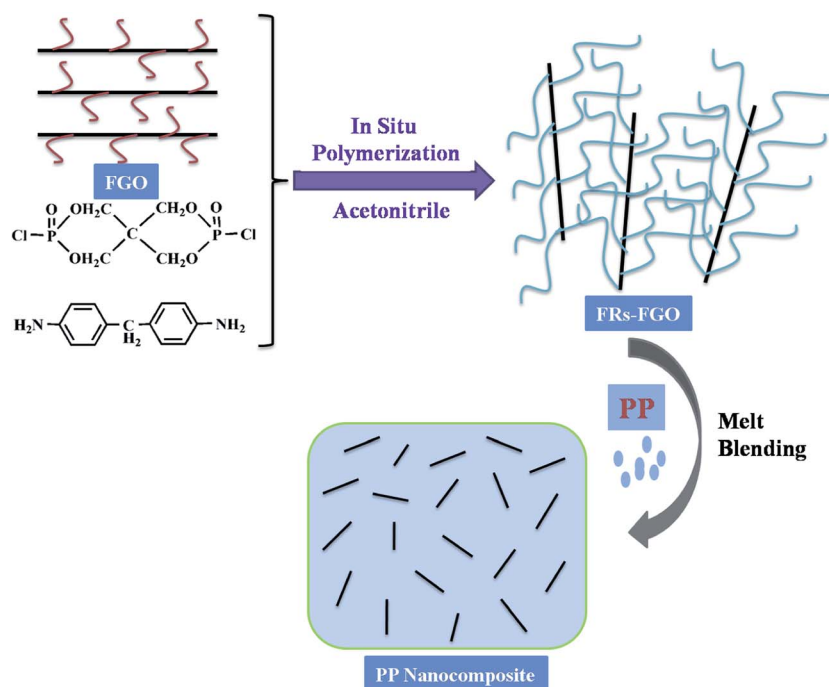
2.3 Preparation of FRs/PP composites and FRs-FGO/PP nanocomposites

The composition of PP and its flame retardant composites are presented in Table 1. Prior to use, PP and PP-g-MA were dried in

a vacuum oven at 80 °C overnight. PP-g-MA was maintained at the same loading of 3 wt% during the preparation of all the composites. Briefly, the PP nanocomposite containing 20 wt% loading of FRs-FGO was prepared as follows: PP, PP-g-MA and FRs-FGO were melt-mixed in a twin-roller mill for 10 min; the temperature of the mill was maintained at 180 °C, and the roller speed was 100 rpm. After mixing, the sample was hot-pressed at about 190 °C under 10 MPa for 10 min into sheets with a thickness of 3.0 mm for characterization. Similar to the procedure described above, the other two samples (PP-1, PP-2) were obtained.

Table 1 Composition of PP and its flame retardant composites

Sample	PP (g)	PP-g-MA (g)	FRs (g)	GO (g)	FRs-FGO
PP-0	100	—	—	—	—
PP-1	77	3	20	—	—
PP-2	77	3	18	2	—
PP-3	77	3	—	—	20



Scheme 2 Schematic illustration of the preparation of PP nanocomposite.

2.4 Characterizations

Fourier transform infrared (FTIR) spectra were obtained using a Nicolet 6700 (Nicolet Instrument Company, USA) spectrophotometer with the wavenumber ranging from 500–4000 cm^{-1} . Samples were mixed with KBr powders and pressed into tablets for characterization. The concentration for the preparation of the pellets was maintained in the range of 0.1–1 wt%.

Wide-angle X-ray diffraction patterns of the samples were recorded on an X-ray diffractometer (Rigaku Dmax/TA), using a Cu K α tube and an Ni filter ($\lambda = 0.1542$ nm) at 40 kV and 20 mA.

X-ray photoelectron spectroscopy (XPS) was conducted on a VG EscalabMark II spectrometer (Thermo-VG Scientific Ltd. UK), using Al K α excitation radiation ($h\nu = 1253.6$ eV). All the XPS spectra were calibrated using the C1s line at 284.8 eV. Curve fitting and background subtraction were achieved using XPS peak fit software.

The morphology and structure of GO, FGO, FRs-FGO and PP nanocomposites were studied by transmission electron microscopy (TEM, JEM-2100F, Japan Electron Optics Laboratory Co., Ltd, Japan) at an acceleration voltage of 100 kV. GO and FGO were dispersed in deionized water under 0.5 h of ultrasonication. FRs-FGO was purified by extracting over DMF, and then dispersed in deionized water. All the obtained dispersions were dripped onto copper grids for observation. These ultrathin sections of PP nanocomposites with a thickness of 50–70 nm were obtained using a CM1900 microtome (Leica, Germany) with water. Then, the ultrathin sections were placed on copper grids before observation.

Thermogravimetric analysis (TGA) was carried out on a TGA-Q5000IR (TA Instruments, USA) thermo-analyzer instrument. About 3.0 mg of the sample was measured from room temperature to 700 $^{\circ}\text{C}$ at a linear heating rate of 20 $^{\circ}\text{C min}^{-1}$ under both air and nitrogen atmosphere (gas flow rate of 150 ml min^{-1}).

The flammability of the samples was investigated by cone calorimeter (Fire Testing Technology, UK) according to ISO 5660. Each specimen, of dimensions 100 \times 100 \times 3 mm, was wrapped in an aluminum foil and exposed horizontally to 35 kW m^{-2} external heat flux.

Thermogravimetric analysis/infrared spectrometry (TG-IR) of the samples was performed using the TGA Q5000 IR thermogravimetric analyzer that was interfaced to the Nicolet 6700 FTIR spectrophotometer. About 5.0 mg of the sample was put in an alumina crucible and heated from 30 to 600 $^{\circ}\text{C}$ at a heating rate of 20 $^{\circ}\text{C min}^{-1}$ (nitrogen atmosphere, flow rate of 45 ml min^{-1}). The stainless steel transfer pipe and gas cell were heated at 230 $^{\circ}\text{C}$ to avoid the condensation of volatile compounds.

Real-time Fourier transform infrared spectra (RT-IR) were recorded using the Nicolet 6700 FT-IR spectrophotometer equipped with a ventilated oven equipped with a heating device. The cured samples were mixed with KBr powders, and the mixture was pressed into a disc with a concentration in the range of 0.1–1.0 wt%, and then placed into the oven. The temperature of the oven was increased at a heating rate of about 10 $^{\circ}\text{C min}^{-1}$.

Raman spectra were carried out on a LabRAM-HR Confocal Raman Microprobe (JobinYvon Instruments, France) in the range of 500–2000 cm^{-1} using a 514.5 nm argon ion laser.

The melting and crystallization behavior of the samples were investigated by differential scanning calorimetry (DSC Q2000, TA Instruments Inc., USA). Isothermal crystallization curves were recorded at 135 $^{\circ}\text{C}$ in nitrogen, while non-isothermal crystallization traces were collected at a cooling rate of 10 $^{\circ}\text{C min}^{-1}$ in nitrogen. Samples (2–5 mg) were heated from room temperature to 180 $^{\circ}\text{C}$ and then cooled to room temperature at a linear rate of 10 $^{\circ}\text{C min}^{-1}$. This heating-cooling cycle was repeated twice.

3. Results and discussion

3.1 Structural and morphological characterization

Fig. 1 shows the XRD patterns of GO, FGO and FRs-FGO. The characteristic diffraction peak of GO is located at $2\theta = 10.3^{\circ}$, corresponding to the (002) reflection of GO.³³ A weak peak at $2\theta \sim 42^{\circ}$ is attributed to the (100) reflection of GO. Upon the chemical modification of GO with DDM, FGO exhibits a diffraction peak at a smaller diffraction angle of 8.64° , suggesting a significant enlargement in interlayer spacing. The enlarged intra-gallery space of GO is attributed to the intercalation of DDM *via* a ring-opening reaction. In the case of FRs-FGO, no visible diffraction peak is observed in XRD patterns, indicating that the FGO sheets are exfoliated or dispersed disorderly in the FRs *via* an *in situ* reaction prior to blending with the polymer matrix. The previously dispersed FGO sheets in FRs can simultaneously facilitate uniform dispersion and improve the interfacial adhesion of FGO in PP.

To further confirm the structure of GO and FGO, X-ray photoelectron spectroscopy (XPS) was performed to investigate the surface composition of GO before and after the modification. The XPS C1s spectra of (a) GO, (b) FGO, (c) FRs-FGO, (d) XPS survey scans of GO, FGO and FRs-FGO are presented in Fig. 2. The relative area percentages, full-width at half-maximum (FWHM) of the different C1s peaks and the atomic percentages of C, O, N and P for GO, FGO and FRs-FGO are summarized in Tables S1 and S2,[†] respectively (see the ESI). As shown in Fig. 2a, GO has a considerable

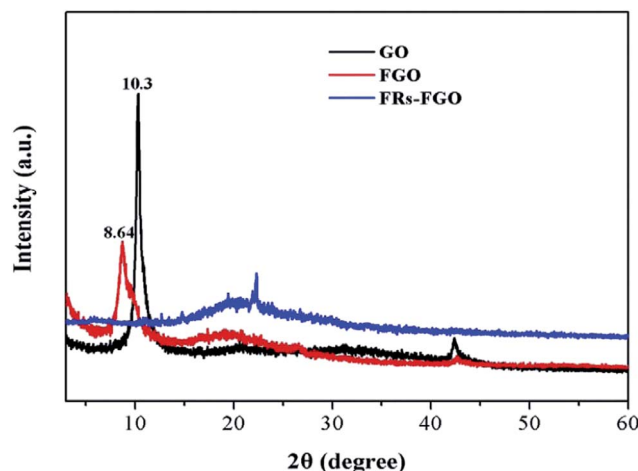


Fig. 1 XRD patterns of GO, FGO and FRs-FGO.

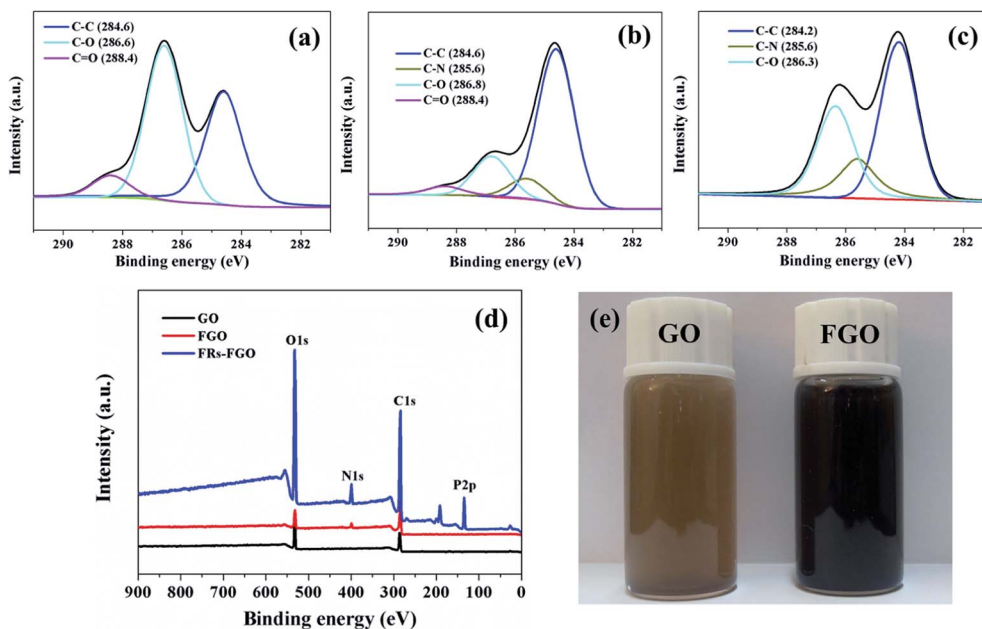


Fig. 2 XPS C1s spectra of (a) GO, (b) FGO, (c) FRs-FGO, (d) XPS survey scans of GO and FGO and (e) digital photos of GO and FGO dispersed in water and DMF, respectively.

degree of oxidation with a C/O atomic ratio of 63.2%/36.8%, and the C1s XPS spectrum of GO can be deconvoluted into four peaks, corresponding to the carbon atoms in different functional groups. Characteristic peaks at 284.6 (FWHM 1.45 eV), 286.6 (FWHM 1.45 eV) and 288.4 eV (FWHM 1.45 eV) are attributed to un-oxidized graphite carbon (C-C), C atoms in hydroxyl and epoxy/ether groups (C-O), and carboxyl groups (O-C=O), respectively.³⁴ After the modification of GO with DDM, the relative peak areas for the oxygen containing groups (64.2%, Table S1[†]) are reduced significantly, especially the peak of C-O for the epoxy group and C=O for the carboxyl group. The reduced relative peak areas for oxygen-containing groups indicate that DDM can not only be grafted on the GO surface but can also partially reduce GO, which was also observed in the previous work.³⁵ Moreover, a new peak at 285.6 eV (C-N) is observed in the C1s spectra of FGO, indicating the successful attachment of DDM to the surface of GO sheets. In the C1s spectrum of FRs-FGO, three types of carbon with different chemical states are observed, which appear at around 284.2 (C-C), 285.6 (C-N) and 286.3 eV (C-O). From the XPS survey scans of GO, FGO and FRs-FGO (Fig. 2d), a new peak (N1s) at 400 eV is observed for FGO compared to pure GO, which further proves the reaction between GO and DDM. In addition to the N1s peak, two new peaks at 191.2 and 134.1 eV attributable to the P2s and P2p, respectively, are present in the XPS spectrum of FRs-FGO.²¹ Based on the XPS C1s spectrum and the survey scans of FRs-FGO, the structure of phosphamide nanocomposites can be verified. To further investigate the structure of GO, FGO, FRs-FGO, the high-resolution O1s spectra of (a) GO, (b) FGO and (c) FRs-FGO and N1s spectra of (d) FGO and (e) FRs-FGO and P2p spectra of (f) FRs-FGO are shown in Fig. S1 (the detailed description and discussion of assignment of XPS peaks are available in

the ESI[†]). To directly observe the reduction of GO, the color changes before and after the reaction are shown in the digital photos of GO and FGO dispersed in water and DMF, respectively (Fig. 2e). Because of the presence of hydrophilic oxygen functional groups on its surface and edge (carboxyl, hydroxyl), GO is easily exfoliated in aqueous media, exhibiting a light yellow color. In the reduction process, the grafting of DDM on the GO surface makes the hydrophilic GO hydrophobic and there are color changes from light yellow GO in water to black, which is considered to be a sign of GO reduction.³⁶

The FTIR spectra of (a) GO, (b) FGO, (c) FRs and (d) FRs-FGO are shown in Fig. 3. It is obvious that some typical absorption peaks of oxygen functional groups appear in the spectrum of GO: O-H stretching vibration (3379 cm^{-1}), C=O stretching vibration in carboxylic acid and carbonyl moieties (1724 cm^{-1}), C=C stretching vibration (1623 cm^{-1}), O-H deformation vibration (1420 cm^{-1}), C-O stretching vibration in carboxylic (1226 cm^{-1}) and C-O-C stretching vibration in epoxy groups (1043 cm^{-1}).³⁷ After the reaction with DDM, FGO displays some new peaks, as shown in Fig. 3b: C-H stretching vibration (2920 cm^{-1} , 2850 cm^{-1}) and aromatic vibration (1580 cm^{-1} , 1510 cm^{-1}) in DDM. The appearance of these new peaks originating from DDM confirms successful modification. Furthermore, the peak at 1043 cm^{-1} attributed to the stretching vibration of epoxy groups could not be detected in the spectrum of FGO because of the nucleophilic substitution reaction between the primary amine group of DDM with the epoxy groups of GO, which further provides evidence for successful functionalization. For the FTIR spectrum of FRs (Fig. 1c), the absorption peaks at 3030 cm^{-1} (unsaturated hydrocarbon), 2850 cm^{-1} ($-\text{CH}_2-$), 1620 cm^{-1} ($-\text{NH}_2$), 1510 cm^{-1} (C=C), 1245 cm^{-1} (P=O), 1027 cm^{-1} (P-O-C) and 1085 cm^{-1} (P-N) are observed,

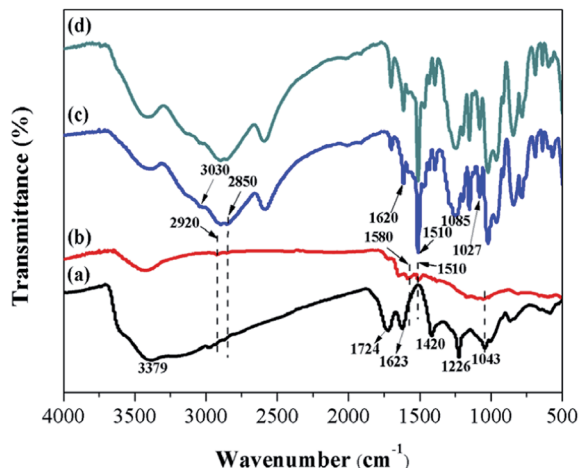


Fig. 3 FTIR spectra of (a) GO, (b) FGO, (c) FRs and (d) FRs-FGO.

which is consistent with the FTIR data previously reported.³¹ In Fig. 3d, the FRs-FGO presents the same absorption peaks as those of FRs because of the overlapping of the peaks of FGO and FRs and the weak absorption intensities of FGO.

The crucial factors affecting the reinforcement of the properties of polymer nanocomposites are dispersion state and the formation of strong interfacial interaction of nano-fillers in the polymer matrix. To observe the morphology and evaluate the dispersion state of GO and FGO in PP matrix, the TEM images of (a) GO, (b) FGO, (c) PP-2 and (d) PP-3 are presented in Fig. 4. As can be seen from Fig. 4a, the morphology of GO is wrinkled and almost transparent, and the surface of GO sheets is fairly smooth. The ultrathin nature of GO sheets makes them nearly invisible, whereas the multilayered stacks of the GO make them relatively clear. In the case of FGO (Fig. 4b), the surface of FGO appears to be rough and slightly fuzzy, which is attributed to the grafting of DDM along with the stacking of GO after reduction. In Fig. 4c, upon the *in situ* incorporation of FGO into

phosphoramidate oligomers, the surface and edge of FRs-FGO sheets are fuzzier than that of FGO. Moreover, a few stacking graphene sheets are clearly observed. The reason for the morphological change in FRs-FGO relative to FGO is that the phosphoramidate is successfully grafted and wrapped on FGO. The dispersed states of GO and FGO in PP are shown in Fig. 4c and d, respectively. GO sheets are dispersed in PP mainly in the form of multilayered stacked structures, and only minor exfoliated structures are observed. The obscure structures are the exfoliated structures and the vivid ones are the stacked structures. In comparison, FGO dispersed in PP sample (Fig. 4d) is much better than those of GO in PP, and the exfoliated structures of FGO are prominent in PP. The improved dispersion of FGO can be attributed to two aspects: the surface modification of GO can improve the dispersion of FGO in common organic solvents and the interfacial interaction with FRs, resulting in the exfoliation of FGO in FRs; *in situ* polymerization is regarded as one of the most effective methods to prepare polymer nanocomposites, which is beneficial in improving the dispersion of FGO in FRs. Therefore, the combination of chemical modification and *in situ* polymerization finally produces PP nanocomposites with homogeneously dispersed FGO.

3.2 Thermal and combustion behaviors

Thermogravimetric analysis (TGA) was employed to evaluate the thermal stability and degradation behaviors of nanofillers and polymer composites. The TGA curves of GO, FGO, FRs, FRs-FGO, PP and its composites under air and nitrogen atmosphere are shown in Fig. 5 and 6, respectively. The initial degradation temperature of samples is the temperature at which 10 wt% mass loss occurs ($T_{0.1}$). The temperature of maximum weight-loss rate (T_{max}) is obtained from the peak maxima of DTG curves. The detailed data obtained from the TGA curves are listed in Table 2.

Under air atmosphere, GO starts to lose weight below 100 °C because of the release of adsorbed water.³⁶ The main mass loss

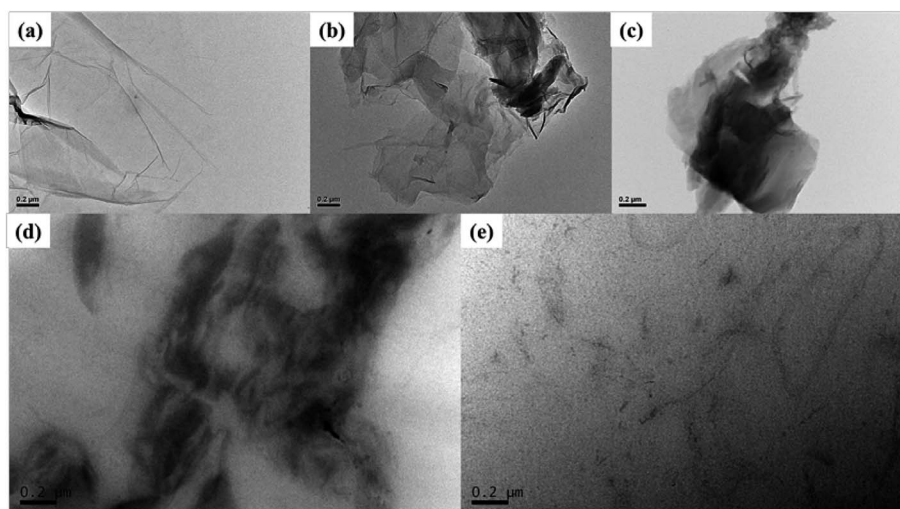


Fig. 4 TEM images of (a) GO, (b) FGO, (c) FRs-FGO, (d) PP-2 and (e) PP-3.

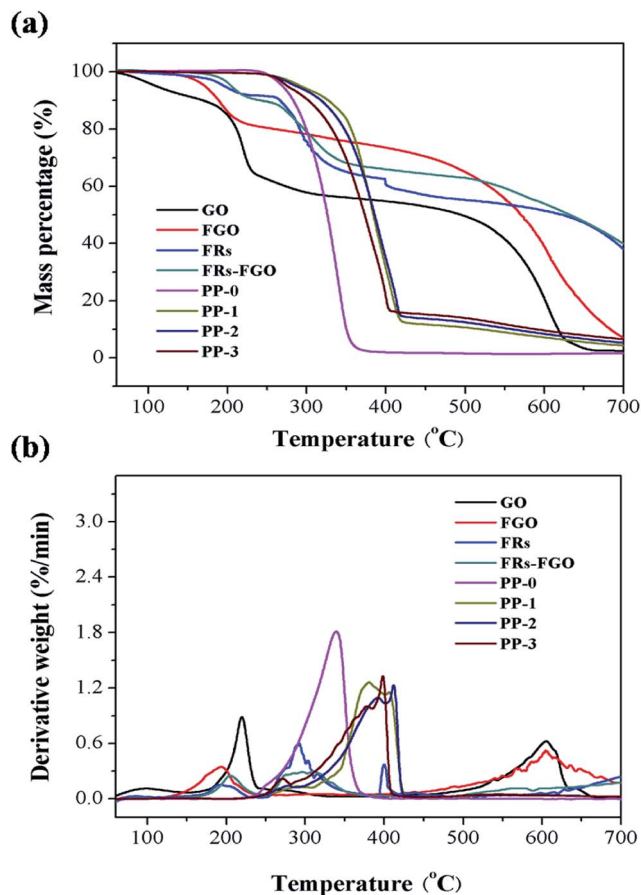


Fig. 5 TGA curves of GO, FGO, FRs, FRs-FGO, PP and their composites under air atmosphere.

of GO has two stages in the temperature ranges of 200–300 °C and 550–650 °C. The first stage is attributed to the decomposition of oxygen-containing groups and the other to the oxidation of char residue. Reduced by DDM, FGO is more stable than GO and exhibits higher initial degradation temperature ($T_{0.1}$) and char residues. In the thermal degradation of FRs, the minor mass loss occurring in the range of 150–250 °C is attributed to the release of water or unreacted monomer. With an increase in temperature, the main decomposition process occurs above 280 °C, where some complex chemical reactions occur, including the scission of phosphate ester bonds and the formation of intumescent char.³¹ The char yield of FRs at 700 °C is as high as 38.1%. The FRs-FGO exhibits similar degradation behaviors as FRs but higher thermal stability with more char residues at 700 °C (39.8 wt%). Pure PP undergoes thermal degradation in the temperature range of around 250–380 °C, which corresponds to the random scission of PP chains. The $T_{0.1}$, T_{max} and char yield of PP is 280 °C, 339 °C and 1.64 wt%, respectively. For the PP composites, the incorporation of flame retardant additives increases $T_{0.1}$, T_{max} and char yields, indicating the improvement of thermo-oxidation resistance. For example, at the FRs-FGO loading of 20 wt%, the $T_{0.1}$, T_{max} and char yield of PP-3 are 302 °C, 398 °C and 6.55 wt%, respectively. The improvement in $T_{0.1}$ is attributed to the release of water or unreacted monomer for

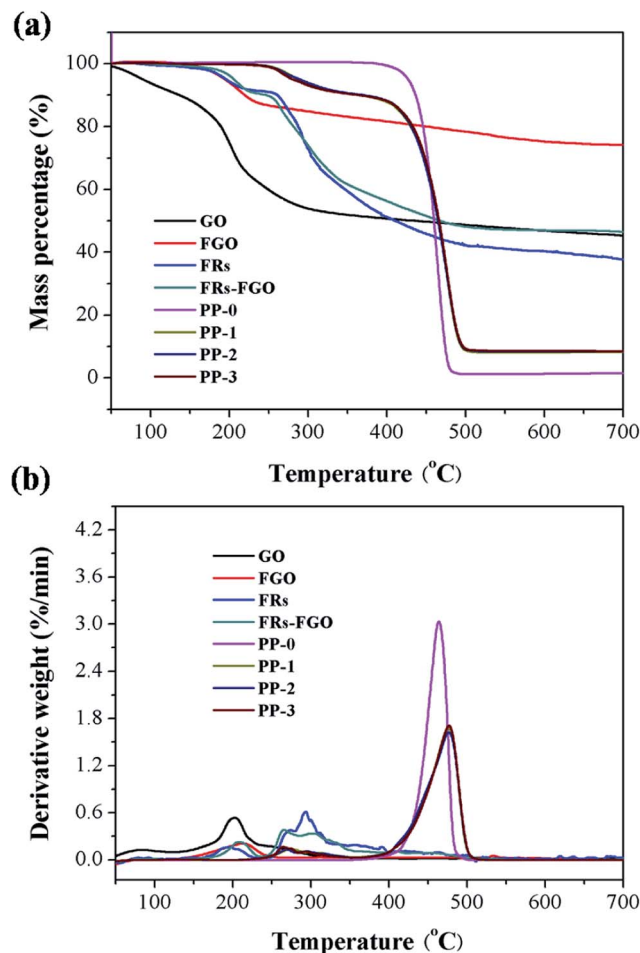


Fig. 6 TGA curves of GO, FGO, FRs, FRs-FGO, PP and their composites under nitrogen atmosphere.

Table 2 TGA data of PP and the resulting PP composites

Sample	$T_{0.1}$ (°C)		T_{max} (°C)		Char (700 °C, wt%)	
	N ₂	Air	N ₂	Air	N ₂	Air
PP-0	436	283	464	339	1.53	1.64
PP-1	365	327	476	381	8.29	4.35
PP-2	370	318	477	412	8.56	5.34
PP-3	364	302	477	398	8.62	6.55

FRs during blending, resulting in higher thermal stability. The higher char residues are attributed to the degradation of phosphorus–nitrogen containing FRs generating more heat-resistant residues. With respect to the char yields of various composites, it is clear that the char residues of PP-3 containing 20 wt% FRs-FGO are higher than those of PP-1 and PP-2. The results indicate that the presence of graphene sheets increases the ratio of graphitic carbon and amorphous carbon among char residues, thus improving the thermal resistance of char residues; significantly better dispersion of FGO in PP than GO leads to a better barrier effect by preventing the escape of pyrolysis products.

As shown in Fig. 6, nanofillers (GO, FGO) and flame retardant additives in nitrogen show similar degradation behaviors because they are heated in air atmosphere. However, nanofillers leave more char residues than those in air atmosphere because of the high thermal stability of char. The virgin PP exhibited an initial decomposition temperature ($T_{0.1}$) of 436 °C, which is higher than PP in air atmosphere. The reason for the lower thermal stability of PP under air atmosphere is that the oxygen promotes the scission of the side chain of PP at low temperature. With the incorporation of additives, the $T_{0.1}$ of PP composites shifts toward lower temperature, which is attributed to the degradation of unstable P–O–C bonds in FRs at low temperature.³⁸ However, the char yield and T_{max} both increase notably, suggesting improved thermal stability at high temperature. High char residues formed during combustion will decrease the release of combustible gas, inhibit heat diffusion and protect the polymer against fire.

Cone calorimetry was used to evaluate the fire performance of these composites. Fig. 7 presents the heat release rate (HRR) and total heat release (THR) *versus* time curves of PP and its composites. Various parameters obtained from cone tests, including time-to-ignition (TTI), peak heat release rate (PHRR),

Table 3 Cone results of PP and its flame retardant composites

Sample	TTI (s)	Peak HRR (kW m ⁻²)	THR (MJ m ⁻²)	TSP (m ²)	FIGRA (kW (m ² s ⁻¹))
PP-0	54	1199	97.8	7.28	22.2
PP-1	69	620	78.5	17.05	9.0
PP-2	64	473	79.0	19.90	7.4
PP-3	66	397	73.9	15.90	6.0

total heat release (THR), total smoke production (TSP) and fire growth rate index (FIGRA) are also summarized in Table 3. It can be observed from Fig. 7a that the pure PP burns very rapidly after ignition and the peak heat rate (PHRR) is as high as 1199 kW m⁻². With the incorporation of 20 wt% FRs, the PHRR of PP-1 decreases significantly to 620 kW m⁻². When the FRs is partially replaced by 2 wt% GO, the PHRR of PP-2 is further reduced to 473 kW m⁻². Compared to PP-1 and PP-2, PP-3 exhibits the lowest PHRR on adding 20 wt% FRs-FGO nanocomposite flame retardant. The PHRR values for PP-1, PP-2 and PP-3 are reduced by 48.3%, 60.6% and 66.9% relative to the pure PP, respectively. Similar to the HRR curves, PP-3 exhibits considerably reduced total heat release (THR) (24.4% reduction), which is significantly lower than those of PP-1 and PP-2. The significant reduction of PHRR and THR for PP-3 can be explained by the fact that FRs, forming a cohesive and compact char layer during combustion, acts as an insulating barrier between fire and PP matrix; FGO sheets act as barriers to prevent the permeation of oxygen and the escape of volatile degradation products. The presence of FGO promotes the formation of graphitic carbon, which reinforces the barrier effect of char layer. As compared with the simple blending of FRs with GO, FRs-FGO performs much better on improving the fire safety properties of PP, which can be attributed to more uniform dispersion and stronger interfacial interaction of FGO in PP than bare GO.

Cone results (Table 3) show that all the composites containing flame retardant additives present prolonged time-to-ignition (TTI) and increased total smoke production (TSP) compared with pure PP. Prolonged TTI suggests that PP composites were harder to ignite than PP, which is probably because of the increased thermal stability of PP composites. The increase in TSP is probably attributed to the incomplete combustion of PP matrix. The fire growth rate index (FIGRA) is used to evaluate the burning propensity of a material, which is calculated as follows: FIGRA = PHRR/time to PHRR. The lower the FIGRA values, the higher the fire safety of materials. Virgin PP exhibits the highest FIGRA value of 22.2 kW m⁻² s⁻¹. As expected, adding flame retardant additives noticeably reduces the FIGRA values of composites and the values follow the sequence: PP-3 (6.0) < PP-2 (7.4) < PP-1 (9.0) < PP-0 (22.2). The lowest FIGRA value for PP-3 containing 20 wt% FRs-FGO among all the composites suggests the lowest burning propensity.

Because the FRs-FGO nanocomposites exhibit superior flame retardant efficiency and good dispersion of graphene, it is

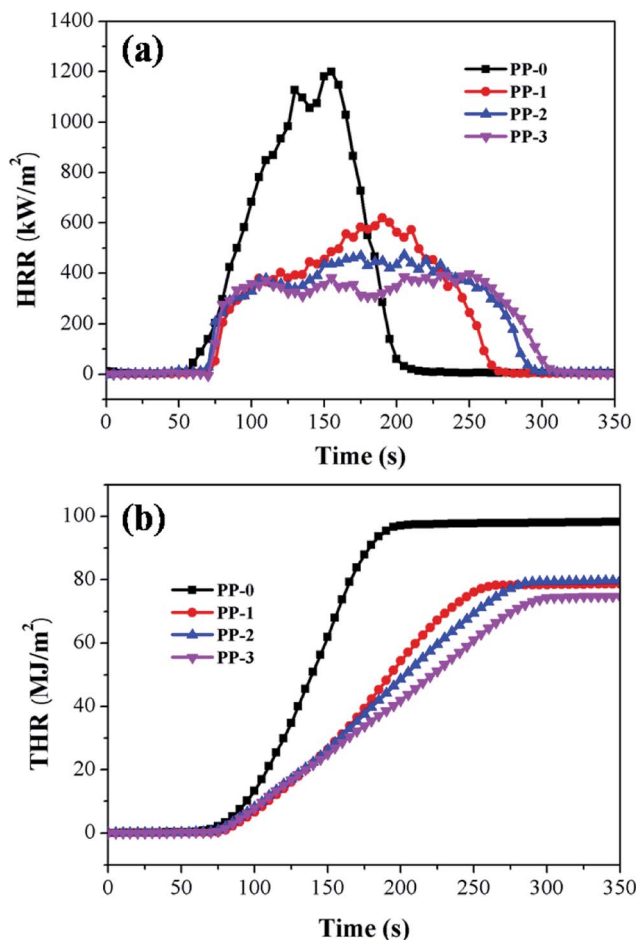


Fig. 7 Heat release rate (HRR) and total heat release (THR) *versus* time curves of PP and its composites.

important to highlight the advantages of this process. The comparison of this composite with other PP-based composites reported in literature in terms of performance and preparation method is summarized in Table S3† (see the ESI).^{39–42} Because of the high heat conductivity of graphene sheets, graphene incorporation led to decreased TTI and slightly decreased THR. However, the FRs-FGO nanocomposites not only increase TTI, but also significantly decrease THR by 24.4%, demonstrating the remarkably enhanced fire safety of PP described in this work. Moreover, the PHRR is also considerably decreased. In general, the dispersion of graphene in polymer matrix *via* the *in situ* polymerization and solvent blending method is better than that of melt blending-based methods. Herein, the graphene sheets were previously exfoliated in flame retardants *via in situ* polymerization, and subsequently incorporated into PP matrix using PP-*g*-MA as a compatilizer by melt blending. As expected, PP/FRs-FGO exhibits much better dispersion than PP-2 by directly melt blending GO in PP.

To investigate the effect of graphene-based nanocomposites flame retardant on the evolved gas products during pyrolysis, TG-FTIR was used to analyze the pyrolysis products. The 3D TG-FTIR spectra of gas phase in the thermal degradation of (a) PP-0 and (b) PP-3 and (c) FTIR spectra of pyrolysis products for PP and PP-3 at the maximum decomposition rate are shown in Fig. 8. As observed from Fig. 8a, the characteristic peaks in the regions of around 2800–3100 cm^{-1} , 1600–1500 cm^{-1} and 1550–1300 cm^{-1} are noted. According to a previous report, the volatilized products are unambiguously identified by characteristic FTIR signals such as C–H compounds (2800–3100 cm^{-1}). For the spectrum of PP-3 (Fig. 8b), the absorptions have no noticeable difference from those of PP-0, which are probably because of the overlapping of the absorptions of the volatile components from FRs. For example, the peaks at around 970 cm^{-1} and 885 cm^{-1} are probably attributed to N–H deformation vibration in NH_3 and P–O stretching vibration, respectively.^{43,44} Similar peaks in the FTIR spectra of the samples indicate a similar composition of the volatile products. In Fig. 8c, the FTIR spectra of the pyrolysis products at maximum decomposition show that the main products of the thermal decomposition of PP-0 and PP-3 are compounds containing hydrocarbons and unsaturated hydrocarbons. The peaks at 2958 and 2920 cm^{-1} , 1645 cm^{-1} , 1460 and 1380 cm^{-1} correspond to the CH_2/CH_3 stretching, C=C stretching and CH_2/CH_3 bending vibrations, respectively.^{43,44}

The absorbance of the pyrolysis products for PP-0 and PP-3 *vs.* time: (a) total, (b) CH_2/CH_3 (c) unsaturated hydrocarbons are presented in Fig. 9. It can be seen that the intensity of pyrolysis products for PP-0 reaches the maximum at about 21.6 min, whereas that for PP-3 reaches the maximum at about 22.2 min. This phenomenon is attributed to the fact that FRs-FGO can improve the thermal stability of PP nanocomposites at high temperature, which is consistent with the TGA results. Moreover, the absorbance intensity of the pyrolysis products for PP composites is significantly lower than that for PP. Consequently, the addition of FRs-FGO can reduce the release of combustible volatiles, and thus leads to reduced heat release rate. The reduced release of organic volatiles during

combustion is attributed to the shielding effect of FGO and char layers and the formation of more char residues.

3.3 Condensed phase analysis

Real time FTIR was employed to investigate the solid pyrolysis products of PP and its composites at various temperatures. The FTIR spectra of PP-0 and PP-3 at different temperatures are presented in Fig. 10 and 11, respectively. PP shows characteristic absorption peaks at 2960, 2920, 2880, 2840, 1460, 1380, 1305, 1255, 1166, 998 and 840 cm^{-1} . At 200 °C, absorptions at 1305, 998 and 840 cm^{-1} , associated with the crystallization of PP, disappear, suggesting the melting of PP crystal.⁴⁵ Meanwhile, the appearance of new peaks at 1720 cm^{-1} resulting from the C=O absorption indicate that PP was oxidized. When the temperature increases up to 300 °C, the relative intensities of all the absorption peaks decrease dramatically, indicating the occurrence of main decomposition. It is worth noting that no obvious absorption is observed at 450 °C, implying that PP decomposes completely. It is clear from Fig. 11 that some new absorption peaks at 1602 cm^{-1} (– NH_2), 1510 cm^{-1} (C=C), 1257 cm^{-1} (P=O), 1025 cm^{-1} (P–O–C) and 1085 cm^{-1} (P–N) appear in the spectra of PP-3 as compared to PP-0.³¹ When the pyrolysis temperature is over 280 °C, the intensity of the peak at 1025 cm^{-1} is sharply decreased because of the decomposition of unstable P–O–C bonds, which is consistent with the TGA results obtained in air. Previous work has reported that phosphate groups will degrade at low temperature to form some phosphoric acid derivatives, which will catalyze polymer degradation to produce more char residues.⁴⁶ Above 330 °C, the rapid decrease in all the peak intensities indicates that the main decomposition occurs. At 450 °C, different from control PP, some specific absorption is observed in the condensed phase of PP-3. The peak at 1290 cm^{-1} assigned to the P=O vibration in P–O–benzene structure indicates the formation of P–O–C complexes with higher thermal stability. Moreover, the appearance of the peaks at 1085 and 880 cm^{-1} resulting from the P–O–P groups confirms the presence of pyrophosphate.³⁸ Hence, the char layer composed of phosphorus–carbon complexes forms during combustion, which acts as an effective barrier for protecting the matrix from decomposing at high temperature.

Raman spectroscopy is a powerful tool for carbonaceous materials to characterize their structures. Fig. 12 shows the Raman spectra of the char residues of PP-1, PP-2 and PP-3. As can be seen from the figure, the Raman spectra of all the samples exhibit two prominent peaks at about 1360 and 1600 cm^{-1} , which correspond to D and G band, respectively. The former is attributed to a breathing mode of *K*-point photons of A_{1g} symmetry, whereas the latter is attributed to the first order scattering of the E_{2g} phonon of sp^2 C atoms.⁴⁷ In general, the ratio of D to G band intensity (I_D/I_G) is employed to estimate the graphitization degree of the char, where I_D and I_G are the integrated intensities of the D and G bands, respectively. A lower ratio of I_D/I_G implies the higher graphitization degree and thermal stability of char structure. For PP-1, the intensity ratio I_D/I_G of the char is about 3.04. The incorporation of GO has a

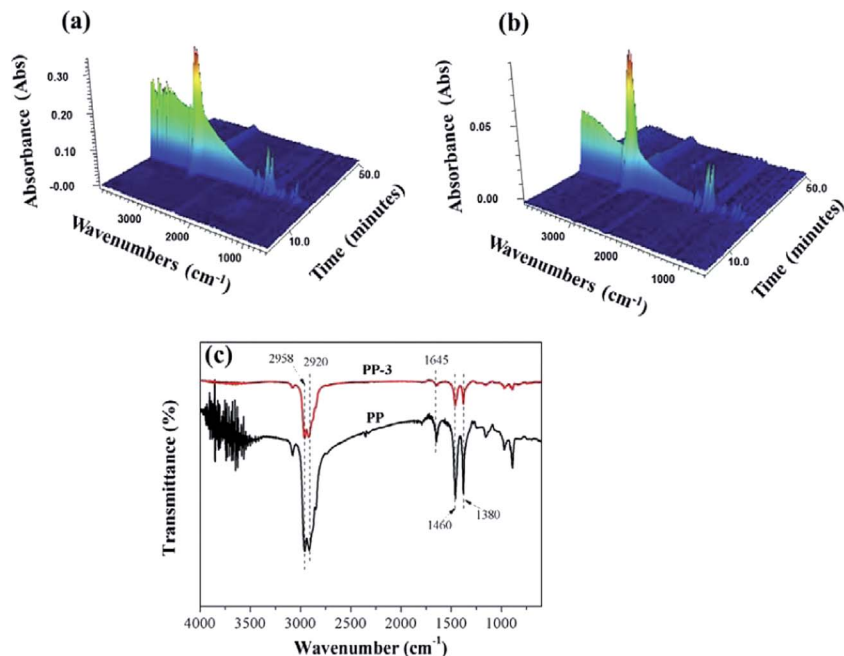


Fig. 8 3D TG-FTIR spectra of gas phase in the thermal degradation of (a) PP-0 and (b) PP-3 and (c) FTIR spectra of pyrolysis products for PP and PP-3 at the maximum decomposition rate.

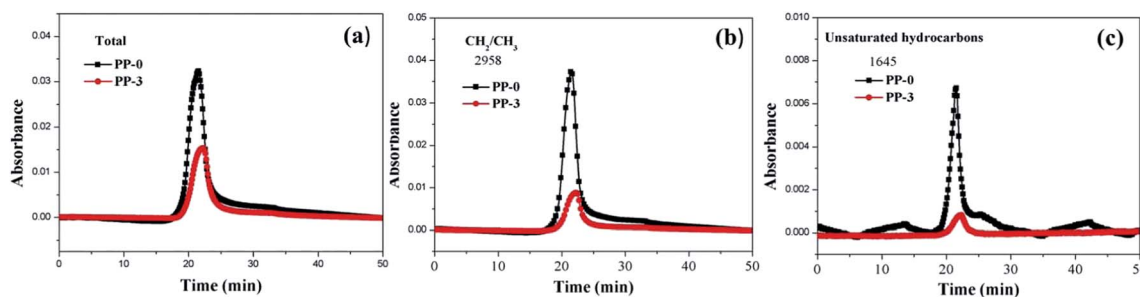


Fig. 9 Absorbance of pyrolysis products for PP-0 and PP-3 vs. time: (a) total, (b) CH_2/CH_3 , (c) unsaturated hydrocarbons.

slight impact on the values of I_D/I_G , whereas the presence of FRs-FGO markedly reduces the I_D/I_G values of the char from PP-3 to 1.85, indicating the increase of graphitized carbons in the residual char. The reduction in I_D/I_G ratio arises from the presence of graphene sheets. The I_D/I_G ratio of PP-2 is much higher than that of PP-3 probably because GO is prone to oxidation under air atmosphere; however, FRs wrapped FGO is more thermally stable because the formation of char from FRs during degradation process prevents the FGO from oxidation.

The effect of various additives on the crystallization behavior of the PP composites was investigated by DSC. Fig. 13 shows (a) non-isothermal crystallization curves (at a cooling rate of $10\text{ }^\circ\text{C min}^{-1}$) and (b) isothermal crystallization (at $135\text{ }^\circ\text{C}$) of PP and its composites. Crystallization temperature (T_c) is the temperature at the crossing point of the tangents of the baseline and the high temperature side of the exotherm. The crystallization peak temperature (T_{cp}) represents the peak temperature of the exotherm, which can be obtained from the non-isothermal crystallization curves (Fig. 13a). As shown in Fig. 13a, the T_c and

T_{cp} of the PP composites (PP-1, PP-2 and PP-3) shift to higher temperature compared with that of the neat PP ($T_c = 115.7\text{ }^\circ\text{C}$, $T_{cp} = 112.4\text{ }^\circ\text{C}$). For example, the T_c and T_{cp} values of PP-1 ($T_c = 123.6\text{ }^\circ\text{C}$, $T_{cp} = 120.0\text{ }^\circ\text{C}$); PP-2 ($T_c = 125.4\text{ }^\circ\text{C}$, $T_{cp} = 121.3\text{ }^\circ\text{C}$); PP-3 ($T_c = 123.9\text{ }^\circ\text{C}$, $T_{cp} = 119.7\text{ }^\circ\text{C}$). The higher T_c and T_{cp} values of PP-1 relative to those of PP-0 can be explained by the fact that FRs act as nucleating agents accelerating the crystallization of PP. The T_c and T_{cp} values of PP-2 are lower than those of PP-3, indicating that GO particles are more efficient in accelerating the crystallization of PP matrix than FGO. GO is an effective nucleating agent compared with FGO because FGO sheets are wrapped by FRs and exfoliated in FRs, which limits their nuclear capability. It is clear from the isothermal crystallization curves (Fig. 9b) that all the additives accelerate the crystallization of the matrix: with the incorporation of 20 wt% additives, the time for complete crystallization is significantly reduced and the time follows the sequence: PP-0 > PP-1 > PP-3 > PP-2. The results are consistent with those obtained from the non-isothermal crystallization curves.

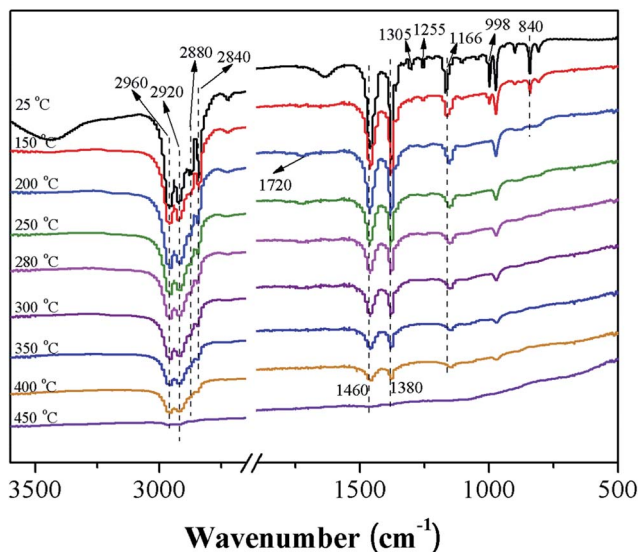


Fig. 10 RT-FTIR spectra of sample PP-0 at different temperatures.

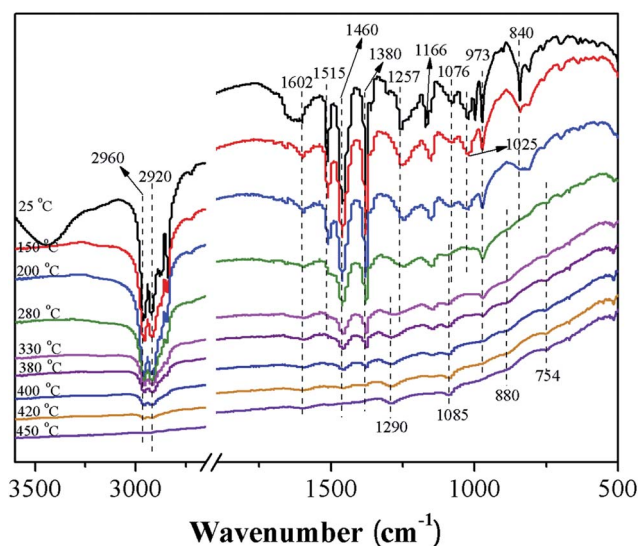


Fig. 11 RT-FTIR spectra of sample PP-3 at different temperatures.

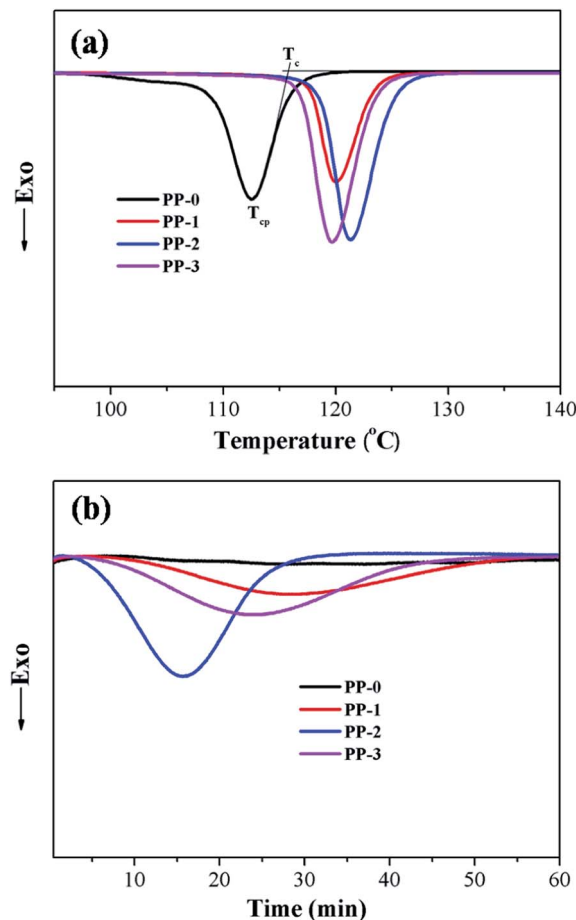


Fig. 13 (a) Non-isothermal crystallization curves (at a cooling rate of $10\text{ }^{\circ}\text{C min}^{-1}$) and (b) isothermal crystallization (at $135\text{ }^{\circ}\text{C}$) of PP and its composites.

4. Conclusion

In conclusion, a novel strategy was demonstrated herein to prepare novel nanocomposite flame retardants (FRs-FGO) containing exfoliated graphene *via in situ* polymerization. Prior exfoliation and the formation of strong interfacial adhesion for FGO in the FRs are the main reasons for the homodispersion of FGO in the PP matrix, as suggested by the TEM images. The FRs-FGO was incorporated into the PP matrix compatibilized with

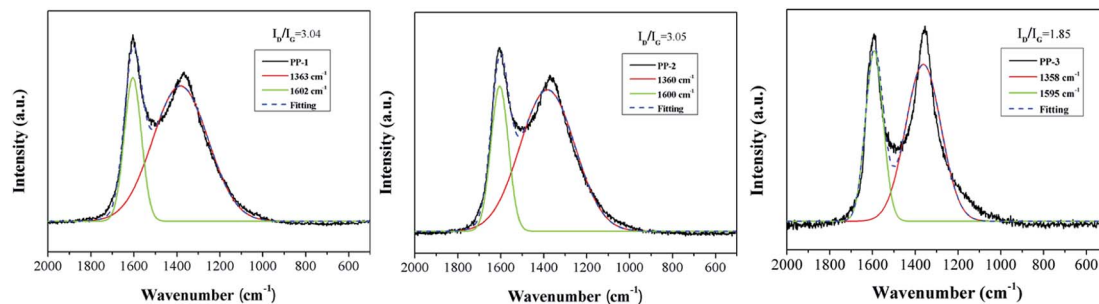


Fig. 12 Raman spectra of char residue of PP-1, PP-2 and PP-3.

PP-grafted maleic anhydride to improve its fire safety. With the addition of 20 wt% FRs-FGO in PP, a significant improvement in thermal stability at elevated temperature with higher char yields was achieved under both air and nitrogen atmosphere. The maximum increase in char yields and T_{\max} was from 1.53 wt% to 8.62 wt% and 339 °C to 398 °C, respectively. Moreover, the fire hazards of the FRs-FGO/PP nanocomposites have also been significantly reduced, including reduced PHRR, THR and FIGRA. The isothermal and non-isothermal crystallization results indicated that FRs-FGO could act as efficient nucleating agents, which can accelerate the crystallization of PP, thus improving the crystallization temperature and decreasing the time for complete crystallization. The approach presented here will provide a promising method to prepare graphene-based nanocomposite flame retardants for the synergistic fire retardancy of polymer materials.

Acknowledgements

This work was financially supported by National Basic Research Program of China (973 Program) (2012CB719701), the joint fund of NSFC and CAAC (no. 61079015), National Natural Science Foundation of China (no. 51303167) and National Natural Science Foundation of China (no. 51203146).

References

- 1 T. Kashiwagi, F. Du, J. F. Douglas, K. I. Winey, R. H. Harris, Jr and J. R. Shields, *Nat. Mater.*, 2005, **4**, 928–933.
- 2 P. a. Song, H. Liu, Y. Shen, B. Du, Z. Fang and Y. Wu, *J. Mater. Chem.*, 2009, **19**, 1305.
- 3 M. Doğan, A. Yilmaz and E. Bayramlı, *Polym. Degrad. Stab.*, 2010, **95**, 2584–2588.
- 4 B. Li and M. Xu, *Polym. Degrad. Stab.*, 2006, **91**, 1380–1386.
- 5 P. Song, Y. Shen, B. Du, M. Peng, L. Shen and Z. Fang, *ACS Appl. Mater. Interfaces*, 2009, **1**, 452–459.
- 6 Q. Li, P. Jiang and P. Wei, *J. Polym. Sci., Part B: Polym. Phys.*, 2005, **43**, 2548–2556.
- 7 F. Gao, L. Tong and Z. Fang, *Polym. Degrad. Stab.*, 2006, **91**, 1295–1299.
- 8 Y. Liu, Y. Zhang, Z. Cao and Z. Fang, *Ind. Eng. Chem. Res.*, 2012, **51**, 11059–11065.
- 9 J. Zhan, L. Song, S. Nie and Y. Hu, *Polym. Degrad. Stab.*, 2009, **94**, 291–296.
- 10 Y. Kopelevich and P. Esquinazi, *Adv. Mater.*, 2007, **19**, 4559–4563.
- 11 C. Lee, X. Wei, J. W. Kysar and J. Hone, *Science*, 2008, **321**, 385–388.
- 12 S. Stankovich, D. A. Dikin, G. H. Dommett, K. M. Kohlhaas, E. J. Zimney, E. A. Stach, R. D. Piner, S. T. Nguyen and R. S. Ruoff, *Nature*, 2006, **442**, 282–286.
- 13 Y. Zhu, S. Murali, W. Cai, X. Li, J. W. Suk, J. R. Potts and R. S. Ruoff, *Adv. Mater.*, 2010, **22**, 3906–3924.
- 14 G. Huang, J. Gao, X. Wang, H. Liang and C. Ge, *Mater. Lett.*, 2012, **66**, 187–189.
- 15 S.-H. Liao, P.-L. Liu, M.-C. Hsiao, C.-C. Teng, C.-A. Wang, M.-D. Ger and C.-L. Chiang, *Ind. Eng. Chem. Res.*, 2012, **51**, 4573–4581.
- 16 X. Qian, L. Song, B. Yu, B. Wang, B. Yuan, Y. Shi, Y. Hu and R. K. K. Yuen, *J. Mater. Chem. A*, 2013, **1**, 6822.
- 17 M. Fang, K. Wang, H. Lu, Y. Yang and S. Nutt, *J. Mater. Chem.*, 2009, **19**, 7098–7105.
- 18 J. Zhu, *Nat. Nanotechnol.*, 2008, **3**, 528–529.
- 19 T. Ramanathan, A. A. Abdala, S. Stankovich, D. A. Dikin, M. Herrera-Alonso, R. D. Piner, D. H. Adamson, H. C. Schniepp, X. Chen, R. S. Ruoff, S. T. Nguyen, I. A. Aksay, R. K. Prud'Homme and L. C. Brinson, *Nat. Nanotechnol.*, 2008, **3**, 327–331.
- 20 W. Gao, L. B. Alemany, L. Ci and P. M. Ajayan, *Nat. Chem.*, 2009, **1**, 403.
- 21 G. Huang, S. Chen, S. Tang and J. Gao, *Mater. Chem. Phys.*, 2012, **135**, 938–947.
- 22 H. J. Salavagione, M. n. A. Gómez and G. Martínez, *Macromolecules*, 2009, **42**, 6331–6334.
- 23 X. Qian, B. Yu, C. Bao, L. Song, B. Wang, W. Xing, Y. Hu and R. K. K. Yuen, *J. Mater. Chem. A*, 2013, **1**, 9827.
- 24 P. Khanra, T. Kuila, N. H. Kim, S. H. Bae, D.-s. Yu and J. H. Lee, *Chem. Eng. J.*, 2012, **183**, 526–533.
- 25 Z. Lei, L. Lu and X. S. Zhao, *Energy Environ. Sci.*, 2012, **5**, 6391.
- 26 Y. Li, B. Li, J. Dai, H. Jia and S. Gao, *Polym. Degrad. Stab.*, 2008, **93**, 9–16.
- 27 Y. Qian, P. Wei, P. Jiang, X. Zhao and H. Yu, *Polym. Degrad. Stab.*, 2011, **96**, 1134–1140.
- 28 D. Y. Wang, A. Das, F. R. Costa, A. Leuteritz, Y. Z. Wang, U. Wagenknecht and G. Heinrich, *Langmuir*, 2010, **26**, 14162–14169.
- 29 M. Doğan and E. Bayramlı, *Polym. Adv. Technol.*, 2011, **22**, 1628–1632.
- 30 X. Wang, L. Song, W. Y. Xing, H. D. Lu and Y. Hu, *Mater. Chem. Phys.*, 2011, **125**, 536–541.
- 31 H. Ma, L. Tong, Z. Xu, Z. Fang, Y. Jin and F. Lu, *Polym. Degrad. Stab.*, 2007, **92**, 720–726.
- 32 W. Hummers and R. Offeman, *J. Am. Chem. Soc.*, 1958, **80**, 1339.
- 33 F.-G. Zhao and W.-S. Li, *J. Mater. Chem.*, 2012, **22**, 3082.
- 34 C. Zhu, S. Guo, Y. Fang and S. Dong, *ACS Nano*, 2010, **4**, 2429.
- 35 Y. Cao, J. Feng and P. Wu, *J. Mater. Chem.*, 2012, **22**, 14997.
- 36 H. L. Ma, H. B. Zhang, Q. H. Hu, W. J. Li, Z. G. Jiang, Z. Z. Yu and A. Dasari, *ACS Appl. Mater. Interfaces*, 2012, **4**, 1948–1953.
- 37 S. Stankovich, R. D. Piner, S. T. Nguyen and R. S. Ruoff, *Carbon*, 2006, **44**, 3342–3347.
- 38 H. B. Liang, A. Asif and W. F. Shi, *J. Appl. Polym. Sci.*, 2005, **97**, 185–194.
- 39 N. N. Hong, Y. Pan, J. Zhan, B. B. Wang, K. Q. Zhou, L. Song and Y. Hu, *RSC Adv.*, 2013, **3**, 16440–16448.
- 40 B. Dittrich, K. Wartig, D. Hofmann, R. Mülhaupt and B. Scharrel, *Polym. Adv. Technol.*, 2013, **24**, 916–926.

- 41 B. Dittrich, K. Wartig, D. Hofmann, R. Mülhaupt and B. Schartel, *Polym. Degrad. Stab.*, 2013, **98**, 1495–1505.
- 42 D. Hofmann, K. Wartig, R. Thomann, B. Dittrich, B. Schartel and R. Mülhaupt, *Macromol. Mater. Eng.*, 2013, **298**, 1322–1334.
- 43 S. A. Hedrick and S. S. C. Chuang, *Thermochim. Acta*, 1998, **315**, 159–168.
- 44 K. Wu, Y. Zhang, W. Hu, J. Lian and Y. Hu, *Compos. Sci. Technol.*, 2013, **81**, 17–23.
- 45 P. Lv, Z. Wang, K. Hu and W. Fan, *Polym. Degrad. Stab.*, 2005, **90**, 523–534.
- 46 S. Zhu and W. Shi, *Polym. Degrad. Stab.*, 2003, **81**, 233–237.
- 47 W. Li, X.-Z. Tang, H.-B. Zhang, Z.-G. Jiang, Z.-Z. Yu, X.-S. Du and Y.-W. Mai, *Carbon*, 2011, **49**, 4724–4730.